Bubble pressure requirements to control the bubbling process in forced co-axial air-water jets

J. Ruiz-Rus[a,b,*], R. Bolaños-Jiménez[a,b], A. Sevilla[c], C. Martínez-Bazán[a,b]

[a] *Área de Mecánica de Fluidos, Departamento de Ingeniería Mecánica y Minera. Universidad de Jaén. Campus de las Lagunillas, 23071, Jaén, Spain.*
[b] *Andalusian Institute for Earth System Research. Universidad de Jaén. Campus de las Lagunillas, 23071, Jaén, Spain.*
[c] *Área de Mecánica de Fluidos, Departamento de Ingeniería Térmica y de Fluidos. Universidad Carlos III de Madrid, 28911, Leganés, Spain.*

Abstract

We analyse the controlled generation of bubbles of a given size at a determined bubbling rate in a co-flowing water stream forcing the gas flow. The temporal evolution of the bubble size, $R(t)$, the air flow rate, $Q_a(t)$, and the pressure evolution inside the bubble, $p_b(t)$, during the bubbling process are reported. To that aim, the temporal evolution of the bubble shape and the pressure inside the air feeding chamber, $p_c(t)$, where a harmonic perturbation is induced using a loudspeaker, are obtained from high-speed images synchronized with pressure measurements. A model is developed to describe the unsteady motion of the gas stream along the injection needle, coupled with the Rayleigh-Plesset equation for the growing bubble, allowing us to obtain $p_b(t)$. Thus, the minimum pressure amplitudes required inside the forming bubble to control their size and bubbling frequency are provided as a function of the gas flow rate, the liquid velocity, u_w, and the forcing frequency, f_f. Two different behaviors have been observed, depending on the liquid-to-gas velocity ratio, $\Lambda = u_w/u_a$. For small enough values of Λ, the critical pressure amplitude is given by $p_s \sim \rho_a \, c \, u_a \, St_f^3$, associated to a rapid pressure increase taking place during an interval of time of the order of the acoustic time. However, for larger values of Λ, $p_s \sim \rho \, u_w^2 \, St_f^3 \, \Lambda^{-1/5} \, We^{-1/4}$. Here ρ and ρ_a are the liquid and gas densities respectively, c the speed of sound in air and $St_f = f_f r_o/u_w$ and $We = \rho u_w^2 r_o/\sigma$ the Strouhal and Weber numbers, where r_o denotes the outer radius of the injector.

Keywords: Bubble formation, bubbling frequency, bubble pressure

---

1. Introduction

The generation of bubbles by injection of a gas stream into a co-flowing liquid is an important problem that has been widely studied (see Chuang and Goldschmidt, 1970; Oğuz and Prosperetti, 1993; Sevilla et al., 2005; Gordillo et al., 2007, among others). This configuration allows the injection of much larger gas flow rates than in the case of releasing gas into a still liquid from a submerged orifice, avoiding the irregular flow regimes and the bubble coalescence (Kumar and Kuloor, 1970; Higuera and Medina, 2006). Maier (1927) was the first to investigate this technique, and documented the decrease of the bubble size when the gas flow was introduced through a cylindrical needle inside an outer laminar liquid co-flow. Later on, Chuang and Goldschmidt (1970) confirmed Maier's observations by performing systematic experiments, and Oğuz and Prosperetti (1993) carried out an exhaustive theoretical and potential flow numerical study of the formation of bubbles using a co-flowing liquid, proposing a scaling law for the bubble size as a function of the co-flow velocity. More recently, Sevilla et al. (2005) and Gordillo et al. (2007), performed a detailed experimental,

---

[*] Corresponding author

Email addresses: `jrrus@ujaen.es` (J. Ruiz-Rus), `rbolanos@ujaen.es` (R. Bolaños-Jiménez), `asevilla@ing.uc3m.es` (A. Sevilla), `cmbazan@ujaen.es` (C. Martínez-Bazán)

theoretical and numerical study of a cylindrical co-flowing configuration in a high-Reynolds-number water jet discharging in a stagnant air atmosphere, characterizing the bubble formation and providing suitable scaling laws for the bubble size and the bubbling time. In a co-axial gas-liquid jet, the bubbling frequency, f_b, is nearly proportional to the liquid velocity, u_w, and inversely proportional to the radius of the gas injector, r_o, giving $f_b \propto u_w/r_o$, with a dependence with the gas flow rate (Rodríguez-Rodríguez et al., 2015). Thus, to produce small bubbles at high frequencies, it is necessary to use very small injectors and large liquid velocities, what limits seriously the use of this simple configuration. To overcome such limitations, it is necessary to force either the liquid or the gas streams to control the bubble generation frequency and the bubble size.

In a recent study, Ruiz-Rus et al. (2020) have reported a new method to control both the size and the frequency of the bubbles generated. Unlike in Ruiz-Rus et al. (2017), where the liquid stream was forced, it consists of forcing the air stream by periodic modulations of the pressure at the upstream air feeding chamber. These authors have showed that, whenever the pressure amplitude is higher than a critical value, the forcing system is able to control the process, leading to the formation of nearly monodisperse bubbles at the forcing frequency, established by the operating conditions. Thus, the bubble size can be decreased by increasing the forcing frequency, f_f, producing bubbles of volume $V_b = Q_c/f_f$, where Q_c is the mean air flow rate. Under effective conditions, two different breakup modes have been reported, referred to as mode M1 and M2 respectively. On the one hand, mode M1 consist of an artificially accelerated natural bubbling regime. Here, bubbles emanate from the tip of an intact ligament smaller than the wavelength of a small interfacial perturbation induced by the oscillating air flow rate, $\lambda_f = u_w/f_f$. Under the M1 mode, both the expansion and the collapse stages of the bubbling process take place faster than in the unforced case due to the air flow modulation induced by the forcing system. On the other hand, bubble breakup under mode M2 takes place from the tip of an air ligament longer than λ_f without having an expansion stage. Ruiz-Rus et al. (2020) characterized the transition from one mode to the other, as well as the length of the intact ligament and the bubble volume, reporting the possibility of reducing the bubble size up to 80% with respect to the unforced cases. The present work will focus on the formation of bubbles under breakup mode M1, analyzing the minimum value of the pressure perturbation that needs to be generated inside the forming bubble to be able to control the forcing process. Consequently, the main goal is to report a quantitative and general criterion for the bubble pressure amplitude, and thus extrapolate the results obtained with our forcing mechanism to other facilities.

The manuscript is organized as follows. The experimental facility, methods and techniques are described in Section 2, while the experimental measurements and results are presented in Section 3. A theoretical model of the forcing process is presented in Section 4, to determine the time evolution of the pressure inside the bubble, $p_b(t)$, the instantaneous gas flow rate, $Q_a(t)$, and bubble volume, $V(t)$, knowing the mean air flow rate, Q_c, and the pressure in the feeding chamber, $p_c(t)$. In Section 5, characteristic scales for the bubble pressure amplitude required to be able to control the bubbling process are provided. Finally, Section 6 is devoted to the main conclusions of the work.

2. Experimental facility and techniques

This section is devoted to describe the experimental facility and techniques used to perform the experimental measurements.

2.1. Description of the experimental facility

The experimental facility, shown in Fig. 1, is the same as that used in Ruiz-Rus et al. (2020), where a detailed description can be found. It basically consists of a co-flowing system to generate bubbles inside a water jet. The air is injected through a short needle of length $L = 17$ mm, and inner and outer radii $r_i = 0.4$ and $r_o = 0.6$ mm, respectively, placed co-axially inside a laminar water jet of radius $r_w = 4$ mm, which discharges into the ambient atmosphere. The needle tip is located at the center of the orifice, so that the air

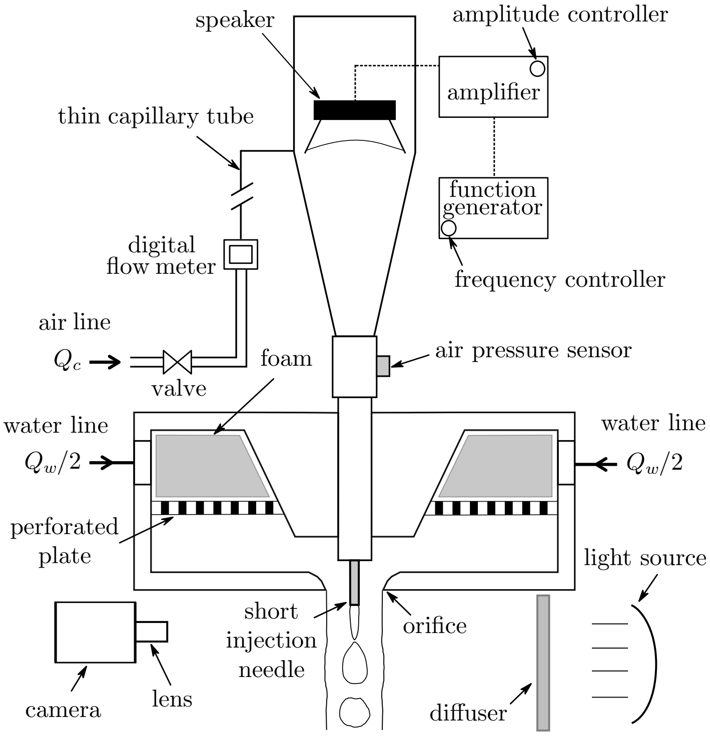

Figure 1: Sketch of the experimental facility including the water and air injection systems. The air stream is forced with a loudspeaker controlled by a function generator and an amplifier.

is released at the centerline of the co-flowing water jet. The apparatus includes a forcing unit to stimulate the air stream by periodically modulating the air injection pressure and, thus, to generate bubbles at the selected forcing frequency, f_f. To that aim, a constant air flow rate, Q_c, is injected through a long capillary tube into the air feeding chamber, placed just upstream of the injection needle, as sketched in Fig. 1. The air chamber, which has a funnel shape to optimize the forcing effect, incorporates a loudspeaker activated by a function generator (model FG110, YOKOGAWA) and a power amplifier (model PA-702, MONACOR). Thus, both the amplitude and frequency of the voltage signal driving the loudspeaker can be precisely controlled to generate the pressure fluctuation inside the chamber, $p_c(t)$, required to produce bubbles at a given rate. Consequently, for a selected pair of values of the air flow rate, Q_c, and water velocity, u_w, bubbles can be generated at a frequency larger than the *natural bubbling* one, f_n, obtained when the bubbling process is not forced (Sevilla et al., 2005; Gordillo et al., 2007).

As recently shown by Ruiz-Rus et al. (2020), there are two different bubble breakup modes depending on the values of the control parameters, respectively denoted modes M1 and M2. In this work, we focus on the breakup mode M1, where bubbles emerge from the tip of an air ligament of length, l_i, smaller than u_w/f_f and, thus the values of the governing parameters were chosen accordingly. Specifically, the water jet velocity was varied in the range $1.36 \leq u_w = Q_w/A_w \leq 1.86$ m/s, where $A_w = \pi(r_w^2 - r_o^2)$ is the water exit cross-section, and Q_w is the water flow rate. The average air velocity at the needle exit, $u_a = Q_c/(\pi r_o^2)$, was modified in the range $1.36 \leq u_a \leq 7.87$ m/s. Finally, the forcing frequency was varied in the range of $250 \leq f_f \leq 500$ Hz. Consequently, both the liquid Reynolds numbers $Re = \rho u_w(r_w - r_o)/\mu \gg 1$, and the air Reynolds numbers $Re_a = \rho_a u_a r_o/\mu_a \gg 1$, so that viscous effects can be neglected in both streams. Here, μ and μ_a represent the liquid viscosity and the air viscosity, respectively. Moreover, the Froude number $Fr = gl_i/u_w^2 \ll 1$, indicating that the effect of gravity is negligible, where l_i denotes the length of the

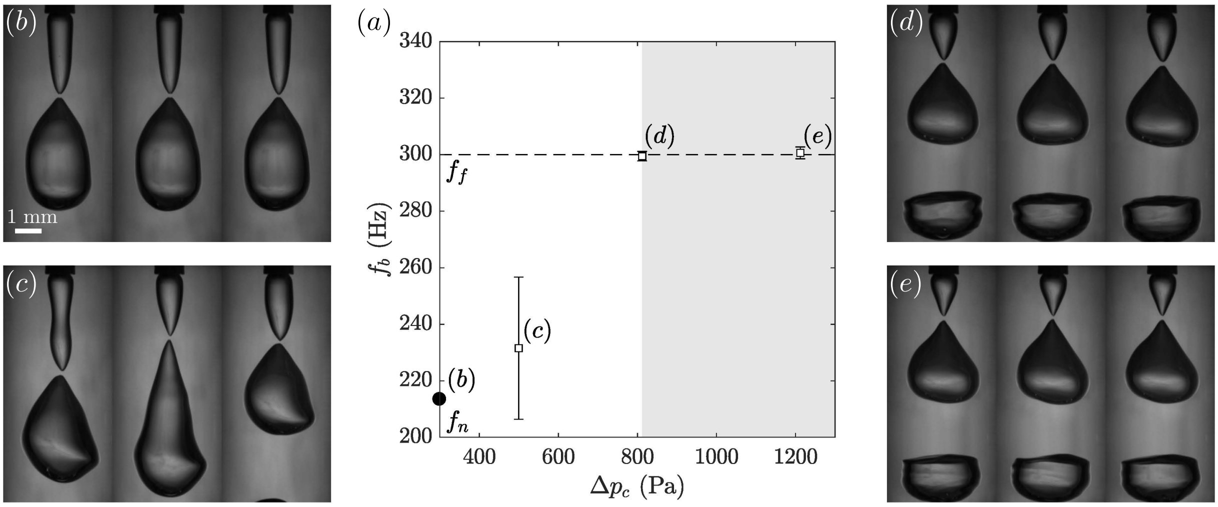

Figure 2: Experimental procedure followed to find the critical pressure amplitude in the chamber, Δp_c^c, for a case where $u_a = 3.8$ m/s and $u_w = 1.36$ m/s, and a forcing frequency $f_f = 300$ Hz. (a) Bubbling frequency, f_b, versus the pressure amplitude in the air feeding chamber, Δp_c. Hollow symbols and bars represent the mean values of f_b and the associated standard deviations for the forced cases, respectively. The black circle indicates the natural bubbling frequency in the unforced case, $f_n = 213$ Hz. The horizontal dashed line indicates the forcing frequency, $f_f = 300$ Hz. The shaded area shows the region corresponding to $\Delta p_c \geq \Delta p_c^c$. The rest of the figures depict images of pinching bubbles at three consecutive cycles of the different cases shown in plot (a). (b) Unforced case ($f_b = f_n$). (c) $\Delta p_c = 500$ Pa $< \Delta p_c^c$. (d) $\Delta p_c^c = 812$ Pa, which corresponds to the *critical* pressure amplitude, leading to the formation of monodisperse bubbles at the forcing frequency. (e) $\Delta p_c > \Delta p_c^c$.

intact ligament, defined as the distance between the needle exit and the position where the bubble pinches off (see Fig. 3). Therefore, the relevant dimensionless control parameters are the forcing Strouhal number, $St_f = f_f r_o / u_w$, the water-to-air velocity ratio, $\Lambda = u_w/u_a$, and the Weber number, $We = \rho u_w^2 r_o/\sigma$.

2.2. Experimental methodology

In the present work, we are interested in determining the minimum or *critical* amplitude of the pressure perturbation that needs to be induced in the air feeding chamber, Δp_c^c, to generate bubbles at the the forcing frequency, $f_b = f_f$. Thus, just to clarify, hereafter f_b will denote the bubble formation frequency, which will be equal to the forcing frequency, f_f, if the bubbling process responds to the forcing system, and $f_b = f_n$ will refer to the bubbling frequency in the unforced natural cases. To characterize the pressure fluctuations inside the feeding chamber, the temporal evolution of the air pressure, $p_c(t)$, was registered by a pressure sensor placed at the bottom of the chamber (see Fig. 1). From this signal, the amplitude of the pressure variation induced in the chamber, Δp_c, could be obtained (see Fig. 4). A data logger was used to synchronize the pressure measurements with the images recorded by a high-speed camera (Photron FASTCAM SA1.1), during the entire bubbling process. These images recorded the temporal evolution of the growing bubble interface allowing us to determine the bubbling frequency f_b (Ruiz-Rus et al., 2020). Spatial resolutions between 23 and 40 μm/pixel were achieved using a Sigma 105 mm macro lens, acquiring images with a frame rate that was varied between 37 500 f.p.s. with a resolution of 192 × 576 pixels, and 45 000 f.p.s. with a 192 × 480 pixel resolution, with a shutter speed of 8.5 μs. A special LED lamp with a light diffuser was used to illuminate the forming bubbles with a backlighting technique.

The critical pressure amplitude, Δp_c^c, was obtained following the procedure illustrated in Fig. 2. In the case shown in the figure, the aim was to generate bubbles at 300 Hz with an air stream velocity of $u_a = 3.8$ m/s and a water jet velocity of $u_w = 1.36$ m/s. Since for these flow conditions the natural bubbling frequency is $f_n = 213$ Hz, a bubble volume reduction of $(1 - f_n/f_f) = 0.29$ (29 %) would be achieved. First, a natural bubbling case was established by setting the values of u_a and u_w, or in dimensionless terms Λ and We, where bubbles were produced at the corresponding natural frequency, f_n (point b in Fig. 2a). The natural case was then forced at a given frequency $f_f > f_n$, introducing a pressure perturbation of amplitude Δp_c with the loudspeaker. As mentioned above, for the case represented in Fig. 2, the natural bubbling frequency was $f_n = 213$ Hz (Fig. 2b), while the forcing frequency was set to $f_f = 300$ Hz. For pressure amplitudes lower than the critical one, $\Delta p_c < \Delta p_c^c$, polydisperse bubbles were irregularly generated in a wide range of frequencies, whose mean value was between the natural and the forcing frequencies, $f_n < \bar{f}_b < f_f$, as shown in the snapshots in Fig. 2(c), associated to point c in Fig. 2(a). The amplitude of the pressure signal was then slowly increased until bubbles were generated periodically at the forcing frequency, $f_b = f_f$ (see Fig. 2d corresponding to point d in Fig. 2a). Thus, when $\Delta p_c \geq \Delta p_c^c$, the forcing system controls the bubbling process, inducing a periodic bubbling regime at the forcing frequency, $f_b = f_f > f_n$ (Fig. 2d), thereby generating smaller bubbles than in the unforced case. Figure 2(d) reveals that the shape of the bubbles formed under effective forcing conditions are different from those produced in the natural case, shown in Fig. 2(b). It is important to note that, for $\Delta p_c \geq \Delta p_c^c$, the bubbles pinch off closer to the needle as Δp_c increases (Fig. 2e), although their sizes do not vary since they are generated at the forcing frequency, $f_b = f_f$.

From the preceding discussion it is clear that finding the dependence of Δp_c^c with the control parameters is important for the practical use of the forcing technique. Thus, for each natural case, the procedure described above was followed for increasing values of f_f, unveiling the dependence of Δp_c^c with u_a, u_w and f_f. We will like to emphasize that all the experimental results corresponding to forced cases reported hereafter have been stimulated at the critical pressure amplitude, $\Delta p_c = \Delta p_c^c$.

Additionally, to experimentally characterize the bubbling process, the growing bubbles were detected from the images taken with a high-speed camera, similar to those shown in Fig. 3. An in-house image processing algorithm based in MATLAB® was used to detect the bubble contour at each frame (see Ruiz-Rus et al., 2020, for further details). This allowed us to obtain the time evolution of the instantaneous volume of the growing bubbles, $V(t)$, assuming that they were axisymmetric, as $V(t) = \int_0^{z_t} \pi D^2(z,t)/4 \, \mathrm{d}z$, where $D(z,t)$ is the diameter of the interface at a given axial coordinate, z, measured from the injector exit, and z_t is the axial position of the bubble tip. Once the bubble volume was determined, its equivalent radius, $R(t)$, was established as the radius of an equivalent spherical bubble, $R(t) = [3V(t)/(4\pi)]^{1/3}$. In addition, the temporal evolution of the instantaneous gas flow rate feeding the bubble was also calculated as $Q_a(t) = \mathrm{d}V/\mathrm{d}t$. To corroborate the accuracy of the bubble volume measurements, the final volumes of the bubbles, experimentally obtained integrating $Q_a(t)$ during the bubbling time, $V_b = \int_0^{1/f_b} Q_a(t)\, dt$, were compared with the volume of air injected during their forming time, $V_b = Q_c/f_b$, obtaining very good agreements.

3. Experimental measurements

Figure 3 shows the time evolution of the bubble formation process of three different forced bubbling cases where $\Delta p_c = \Delta p_c^c$, $We = 15.41$, $St_f = 0.132$ and three air velocities, i.e. $\Lambda = 0.256$ in Fig. 3(a), $\Lambda = 0.358$ in Fig. 3(b) and $\Lambda = 0.773$ in Fig. 3(c). It can be observed that, since in the three cases the water velocity and the forcing frequency are the same, the bubble volume decreases as the air velocity is reduced (Λ increases). It also reveals that the sequence of events taking place during one bubbling period resembles the natural case described by Sevilla et al. (2005), which may be summarized as follows. Just after the pinch-off of a bubble (frames labelled I in the first column of Fig. 3), a new cycle begins with an *expansion stage*, where the air stem that remains attached to the needle, denoted *intact ligament*, inflates radially due to the rapid increase of pressure inside the bubble (II), inducing an outward radial acceleration in the surrounding liquid. As the bubble grows, the pressure inside the bubble decreases until eventually drops below the pressure of the outer liquid, which is nearly the atmospheric one, p_a (Sevilla et al., 2005; Gordillo et al., 2007). At this point, the bubble interface decelerates and the radial expansion velocity of

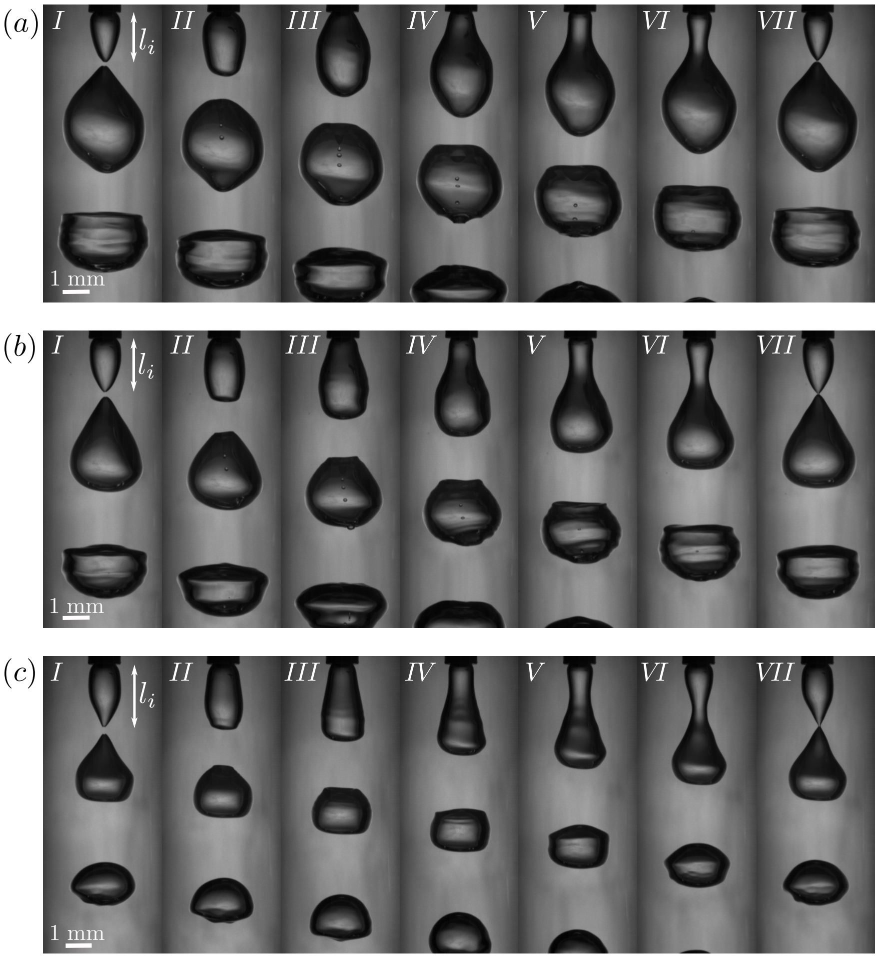

Figure 3: Experimental images showing the temporal evolution of the forced bubbling process corresponding to $f_f = 300$ Hz, $u_w = 1.36$ m/s ($St_f = 0.132$, $We = 15.41$) at three air velocities, (a) $u_a = 5.32$ m/s ($\Lambda = 0.256$), (b) $u_a = 3.80$ m/s ($\Lambda = 0.358$) and (c) $u_a = 1.76$ m/s ($\Lambda = 0.773$). The time interval between the snapshots is 0.56 ms.

the bubble decreases. This pressure difference deforms locally the air-water interface near the injector (III) and eventually becomes parallel to the needle (IV), establishing the onset of the *collapse stage*, where an incipient neck appears. During the collapse phase, the neck moves downstream at the water velocity and accelerates towards the symmetry axis until it finally closes (VII). The length of the intact ligament, l_i, is smaller in the forced cases than in the corresponding unforced ones, and l_i decreases as f_f increases. In fact, the bubbling time is determined by $1/f_f$, and, for constant values of u_a and u_w, the collapse process is faster for increasing forcing frequencies (Ruiz-Rus et al., 2020). Another interesting evidence extracted from Fig. 3 is that the shape of the forming bubbles is nearly spherical for small values of Λ (Fig. 3a), while it becomes more elongated and the bubble pinch-off takes place at larger distances from the needle, as Λ increases (Fig. 3c) (Ruiz-Rus et al., 2020).

Figure 4 shows the temporal evolution of the air pressure in the chamber registered by the pressure sensor, $p_c(t)$ (Figs. 4a, b and c), and the instantaneous gas flow rate, $Q_a(t)$ (Figs. 4d, e, and f), for the cases reported in Fig. 3. The figure also indicates the instants corresponding to the pictures shown in Fig. 3 for clarity. In addition, the end of the expansion stage, estimated as the bubbling time minus the duration

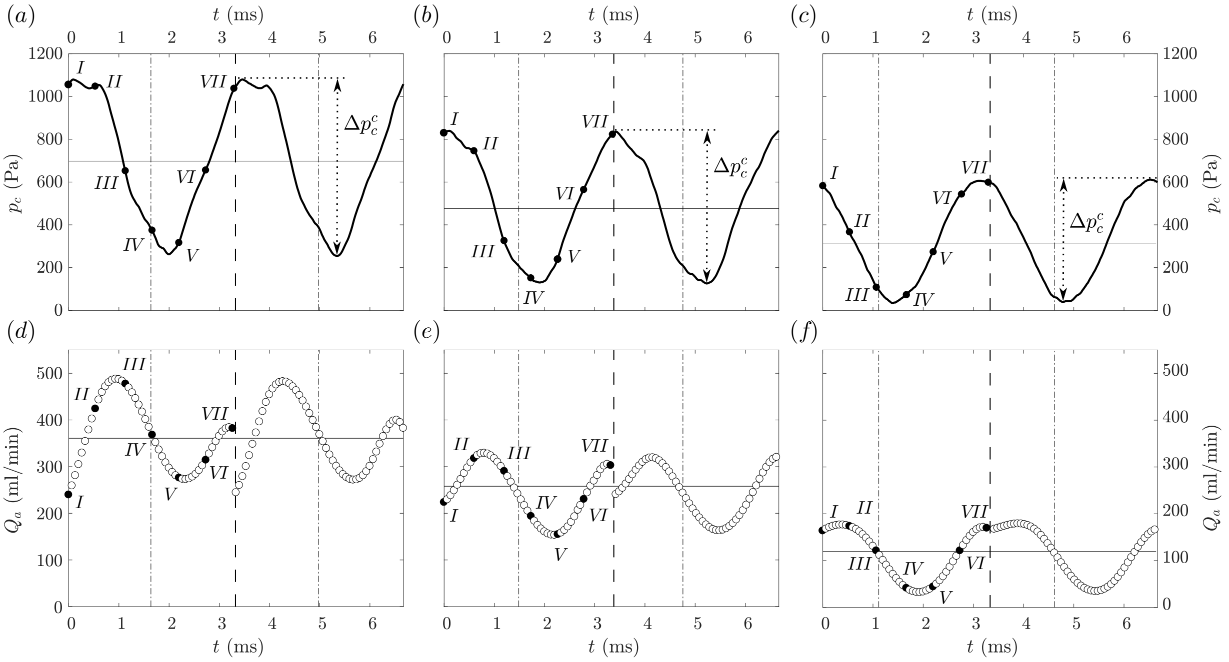

Figure 4: Temporal evolution of the pressure inside the air feeding chamber, $p_c(t)$, (top row) and the instantaneous gas flow rate obtained from the experimental images, $Q_a(t)$, (bottom row) for the conditions reported in Fig. 3 ($We = 15.41$, $St_f = 0.132$). Only one out of three experimental points are plotted for clarity. Panels (a) and (d) correspond to $\Lambda = 0.256$ (Fig. 3a), panels (b) and (e) to $\Lambda = 0.358$ (Fig. 3b), and panels (d) and (f) to $\Lambda = 0.773$ (Fig. 3c). The vertical dashed line in each panel denotes the pinch-off instant while the dash-dotted line separates the expansion and the collapse stages. The figure also indicates the instants corresponding to the images shown in Fig. 3 by the points I, II, III, IV, V, VI and VII in each plot.

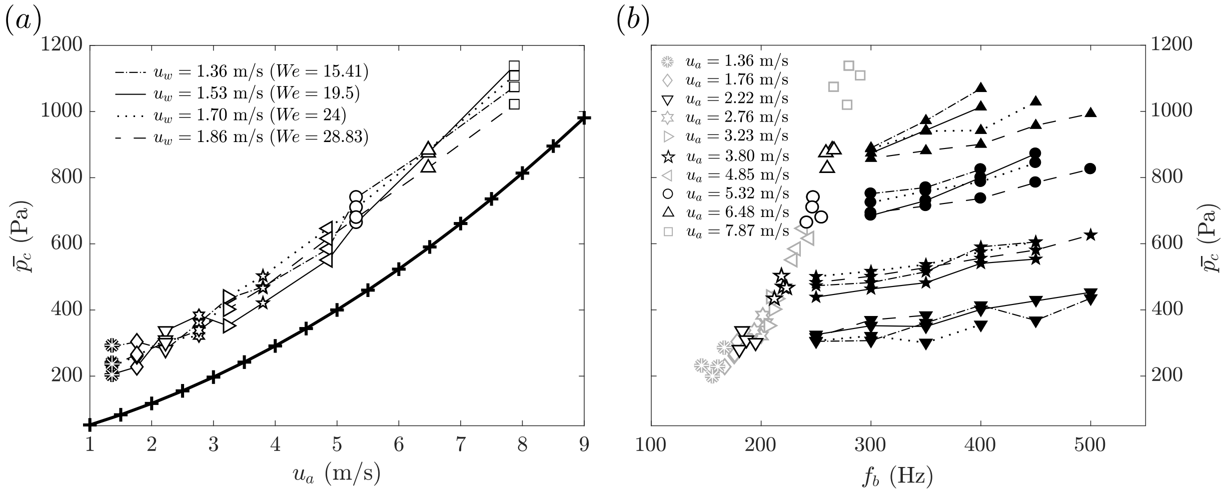

Figure 5: (a) Dependence of the mean pressure in the air feeding chamber with the air velocity for the unforced cases. The thick solid line with crosses represents measurements of the chamber pressure when a steady air stream discharges into an air environment as a free jet. (b) Dependence of $\bar{p_c}$ with the bubbling frequency, f_b. The hollow symbols correspond to the unforced cases shown in (a) and the solid symbols to forced cases where $f_b = f_f$.

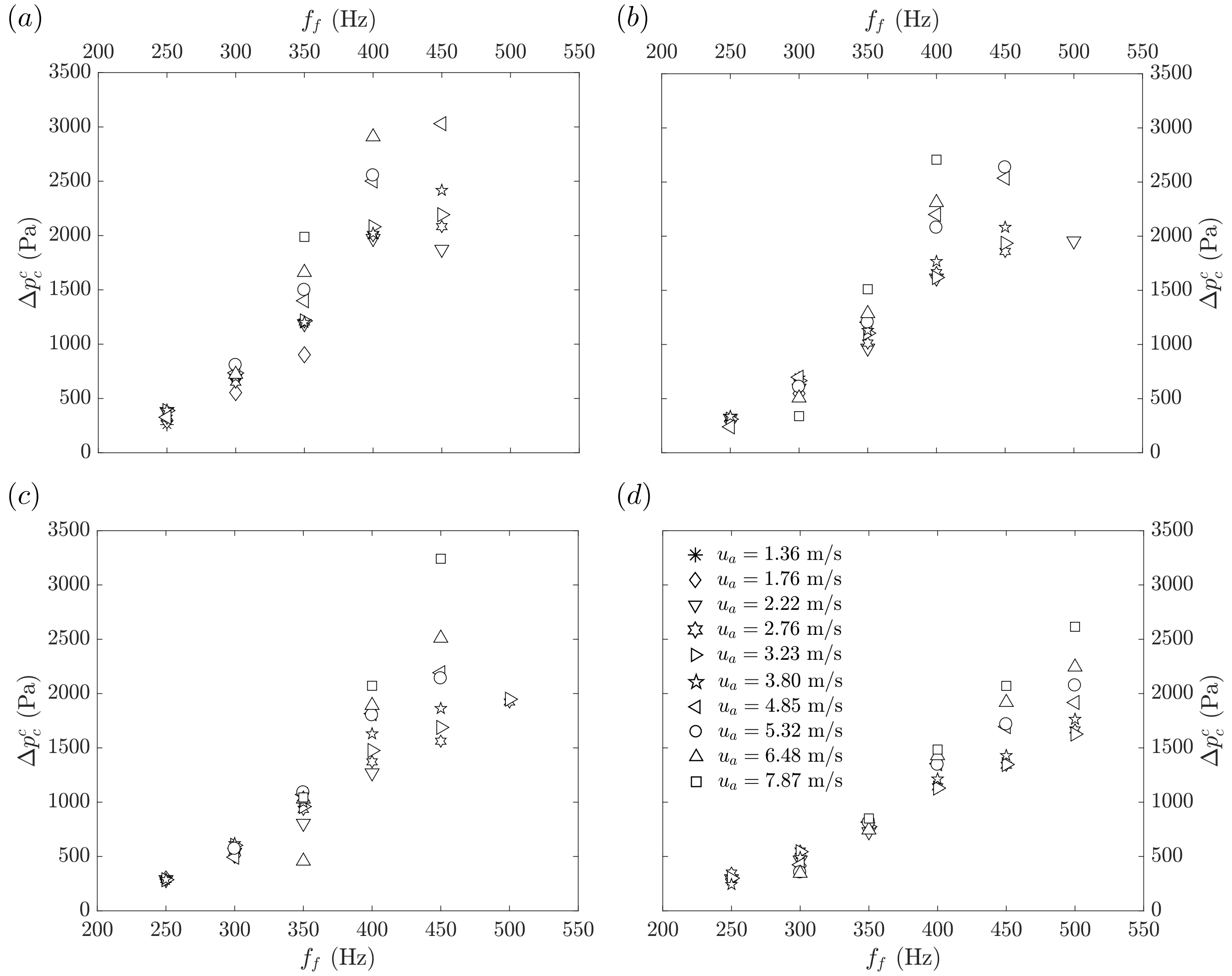

Figure 6: Critical pressure amplitude in the air chamber, Δp_c^c, as a function of the forcing frequency for different values of the air velocity and (a) $u_w = 1.36$ m/s ($We = 15.41$), (b) $u_w = 1.53$ m/s ($We = 19.50$), (c) $u_w = 1.70$ m/s ($We = 24$), (d) $u_w = 1.86$ m/s ($We = 28.83$). The symbols correspond to values averaged over a minimum of 20 bubbling events. The associated standard deviations, plotted as error bars, are smaller than the symbol size in all cases and have not been displayed.

of the collapse stage, $t_{\exp} \simeq 1/f_f - l_i/u_w$, is indicated by a dash-dotted line. Here, it has been taken into account that, since the collapsing neck moves at the water velocity, the length of the intact ligament is given by $l_i \simeq u_w t_{\mathrm{col}}$, where t_{col} is the collapse time (Sevilla et al., 2005; Ruiz-Rus et al., 2020). Figure 4 reveals that $p_c(t)$ is a nearly-harmonic signal at the forcing frequency, reaching its maximum value at the beginning and end of the bubbling cycle. This behaviour was observed for all the effectively forced bubbling regimes in the breakup mode M1 considered herein, indicating that the bubble pinch-off is synchronized with the maximum pressure in the air feeding chamber. Notice that, after the formation of a bubble, $p_c(t)$ starts to decrease, reaching a minimum value around the end of the expansion stage, and then increases again until the bubble pinches off.

The variation of the chamber pressure induces a modulation of the instantaneous gas flow rate feeding the bubble, $Q_a(t)$. Generally, Figs. 4(d), (e) and (f) show that $Q_a(t)$ increases during the initial growth of the bubble because its radial expansion demands an increasing flow rate to satisfy $dV(t)/dt = Q_a(t)$, being larger than the average one, $Q_c = f_f \int_0^{1/f_f} Q_a(t)\,\mathrm{d}t$, during the expansion stage. After reaching its maximum value, $Q_a(t)$ starts to decrease, coinciding with the decrease of the feeding chamber pressure, and becoming smaller than Q_c. During the collapse stage, the pressure in the feeding chamber increases, leading to an increase in $Q_a(t)$ and the closure of the neck. Note that, the relationship between $p_c(t)$ and $Q_a(t)$, which involves the unsteady air flow through the injection needle, will establish the pressure inside the forming bubble, which is different from that in the feeding chamber, and will be the topic of Sect. 4. An inspection of the time evolutions of $Q_a(t)$ in Figs. 4(d), (e) and (f) reveals that they suddenly decrease from the end of each cycle, a behavior not observed in the evolutions of $p_c(t)$ shown in Figs. 4(a), (b) and (c). Indeed, when a bubble pinches off, there is a quick closure of the neck that generates a rapid increase of pressure inside the intact ligament (Sevilla et al., 2005). Such pressure increment, which *a priori* can be considered of the order of $\rho_a c u_a$, where c is the speed of sound in air, stops the flow rate exiting the injection needle and initiates the radial expansion of the bubbles. In fact, Figs. 4(d), (e) and (f), show that the sudden decrease of $Q_a(t)$ from one cycle to the following one is more noticeable at lower values of Λ or, similarly, at large values of u_a, indicating that the pressure increase inside the bubble results larger at lower values of Λ. This reasoning can be further corroborated in Fig. 4(f) where the value of Λ is sufficiently large to have a slow closure of the neck and thus, generate a bubble overpressure lower than that produced by a *water hammer* mechanism. The initial sudden increase of pressure that appears inside the bubbles at low values of Λ causes the rapid radial expansion of the bubble interface observed in Fig. 3(a). This result, together with the fact that the bubbles pinch off closer to the injection needle at low values of Λ (Ruiz-Rus et al., 2020), make the bubble growth evolution more spherical than at higher ones.

The time evolutions of $p_c(t)$ shown in the top row of Fig. 4 indicate that, as in the case of $Q_a(t)$, their mean values and amplitudes decrease as Λ increases, i.e. as u_a is reduced. This result implies that both the mean value and the minimum pressure amplitude required in the air feeding chamber to generate bubbles at the forcing frequency, $f_b = f_f$, increase with the air flow rate. Similar results have been also observed in the unforced cases shown in Fig. 5(a), where the mean pressure increases with the air velocity and barely depends on the water velocity, reflecting the influence of the air pressure drop along the injection needle (Oğuz and Prosperetti, 1993; Gordillo et al., 2007). In fact, the mean pressure in the chamber is higher when the air jet discharges in a water stream, generating bubbles, than when it discharges directly into an air environment as a free jet. Such pressure increment is directly related to the pressure variations inside the bubble due to its growth dynamics, as reported by Sevilla et al. (2005). Furthermore, for constant values of the air velocity, the mean pressure in the chamber increases with the forcing frequency, as displayed in Fig. 5(b). This pressure increase is caused by the effects of the accelerated bubble growth dynamics, as well as by the pressure drop in the needle due to the pulsatile flow, which is greater as the amplitude of the pressure perturbation increases (Yellin and Peskin, 1975).

Figure 6 shows the experimentally determined critical pressure amplitude, Δp_c^c, versus the forcing frequency for several values of the water and air velocities. It can be observed that, for given values of u_w and u_a, Δp_c^c increases with f_f. The influence of u_a is more intricate; in general, Δp_c^c increases with u_a, especially at high forcing frequencies. However, it is almost independent of u_a, or even decreases, at lower values of f_f (see for example in Fig. 6(d), where the critical amplitude is larger for u_a= 3.23 m/s than for u_a= 6.48 m/s). This non-monotonic effect of u_a is due to the coupling of the forcing effect with the dynamics of the growing bubble. Moreover, there is an effect of the injection needle on Δp_c^c, that will be analyzed in Sect. 4. Finally, note that Δp_c^c is a decreasing function of u_w for given values of f_f and u_a, as deduced by comparing the data with the same value of u_a in Figs. 6(a) and 6(d).

At this point, it is worth emphasizing that one of our main goals is to characterize the critical conditions required to achieve an effectively forced bubbling regime, depending on the values of u_a, u_w and f_f. However, it is also important to determine the pressure fluctuations inside the forming bubble when the bubbles are generated at the forcing frequency. In fact, the results shown in Fig. 6 are specific of our particular experimental set-up, but a characterization of the critical amplitude of the pressure inside the bubble would be independent of the forcing system as well as of the gas feeding line (Oğuz and Prosperetti, 1993; Gordillo et al., 2007; Rodríguez-Rodríguez et al., 2015). As a first step towards this goal, the time evolution of $p_b(t)$,

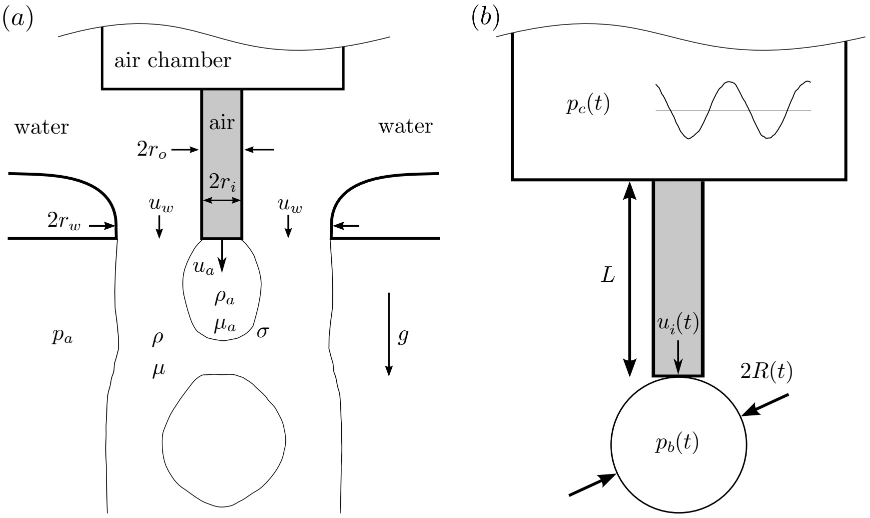

Figure 7: (a) Sketch of bubbling process together with the physical and geometrical parameters. (b) Representation of the injection system coupled with a spherical forming bubble.

whose direct measurement is not possible, must be related with that in the feeding chamber, $p_c(t)$. To this end, a theoretical model is proposed in next section that allows obtaining the pressure inside the bubble.

4. Modeling of the forcing effect

In this section a minimal model aimed at obtaining the pressure inside the growing bubble, $p_b(t)$, from the time evolution of the pressure in the feeding chamber, $p_c(t)$, together with the high-speed recordings, will be described. Figure 7(a) shows a sketch of the injection region of the facility with the main physical and geometrical parameters and Fig. 7(b) a representation of the air injection system. The unsteady air stream flows from the feeding chamber, whose pressure, $p_c(t)$, varies with time due to the effect of the loudspeaker, towards the forming bubble through a needle of length L. The pressure inside the bubble, $p_b(t)$, also varies with time and so does the air flow rate, $Q_a(t)$. For simplicity, the bubble shape will be assumed spherical with radius $R(t)$. Since the expansion Reynolds number $\rho R\dot{R}/\mu \gg 1$, where the dot indicates the time derivative, the spherical liquid flow around the growing bubble can be described by means of the inviscid Rayleigh-Plesset equation (Oğuz and Prosperetti, 1993; Gordillo et al., 2007; Rodríguez-Rodríguez et al., 2015),

$$\rho\left(R\ddot{R}+\frac{3}{2}\dot{R}^2\right)+\frac{2\sigma}{R}=p_b(t), \tag{1}$$

where $p_b(t)$ represents the pressure inside the bubble relative to that in the surrounding water far away from the bubble, which can be assumed to be atmospheric (Sevilla et al., 2005). The terms in the l.h.s. of Eq. (1) stand for the liquid inertia and the surface tension, respectively.

In addition, the air pressure inside the bubble, $p_b(t)$, can be related to the air pressure at the feeding chamber, $p_c(t)$, by an appropriate description of the oscillatory air flow through the needle. To that end, we have used the one-dimensional model derived by García et al. (2014),

$$p_b(t)=p_c(t)-\rho_a l\,\frac{\mathrm{d}u_i(t)}{\mathrm{d}t}-\frac{1}{2}\rho_a K u_i(t)\left|u_i(t)\right|, \tag{2}$$

where $u_i(t)=4Q_a(t)/(\pi r_i^2)\neq u_a$ is the instantaneous air velocity inside the needle, $l=l(t)$ is an effective length and $K=K(Re_i,2r_i/L)$ stands for the dissipative loss coefficient, with $Re_i=Re_a r_o/r_i$ being the time-averaged air Reynolds number based on the inner diameter of the needle. The coefficient K represents a lumped loss coefficient accounting for the flow separation and reattachment at the inlet, together with the frictional viscous losses along the needle. However, in the present configuration, the length-to-diameter ratio is not sufficiently large to have a fully-developed flow which, together with the oscillatory nature of the flow, implies that K might also vary with time. Nevertheless, given the lack of published experimental data considering time-varying pressure loss coefficients, cycle-averaged values will be adopted here. To that aim, for the injection needle used in this study, with $L/(2r_i) = 21.25$, an expression of K as a function of Re_i has been empirically obtained for the range of Reynolds numbers analyzed here, $Re_i < 1500$, providing $K \approx 8.25 - 50.46 \times 10^{-4} Re_i$. The values of K determined by this correlation are similar to those extrapolated from the widely used expression given by Lichtarowicz et al. (1965) for ranges of $L/(2r_i)$ from 2 to 10 and for Re_i from 10 to 20000.

Furthermore, since the bubble growing from the needle tip is considered to be spherical, the instantaneous air flow rate can be expressed in terms of the bubble radius R as

$$Q_a = \frac{\mathrm{d}}{\mathrm{d}t}\left(\frac{4}{3}\pi R^3\right) = 4\pi R^2 \dot{R}\,. \tag{3}$$

Therefore, the instantaneous air velocity can be expressed as

$$u_i = \frac{Q_a}{\pi r_i^2} = \frac{4R^2\dot{R}}{r_i^2}, \tag{4}$$

and, consequently,

$$\frac{\mathrm{d}u_i}{\mathrm{d}t} = \frac{4}{r_i^2}\left(2R\dot{R}^2 + R^2\ddot{R}\right). \tag{5}$$

As a result, by introducing Eqs. (4) and (5) into Eq. (2), the following expression for the air pressure inside the bubble is obtained,

$$p_b = p_c - \frac{4\rho_a l}{r_i^2}\,(2R\dot{R}^2 + R^2\ddot{R}) - \frac{8\rho_a R^4 \dot{R}|\dot{R}|}{r_i^4}\,K. \tag{6}$$

Here, the inertial length $l(t)$ includes the lost-end correction l_o and an effective time-varying length which represents the equivalent length of the slug of fluid ejected under non-irrotational conditions (Cummings, 1986). Its value is obtained by the Cummings' empirical equation, properly adapted to a mean flow with periodic oscillations (Luong et al., 2005), as

$$l(t) = l_o + \frac{3(l_o + L)}{3 + (\mathscr{L}/2r_o)^{1.585}}, \tag{7}$$

being the end correction $l_o \approx \pi r_o/4$ (Rayleigh, 1945; Howe, 1998) and $\mathscr{L}$ the slug effective length,

$$\mathscr{L}(\tau) = \int_0^{\tau} u_i(t)\mathrm{d}t, \tag{8}$$

where τ is the time measured from the beginning of each cycle until the end of the expansion stage.

Combining Eqs. (1) and (6) one gets,

$$\rho\left(R\ddot{R} + \frac{3}{2}\dot{R}^2\right) + \frac{2\sigma}{R} = p_c - \frac{4\rho_a l}{r_i^2}\,(2R\dot{R}^2 + R^2\ddot{R}) - \frac{8\rho_a R^4 \dot{R}|\dot{R}|}{r_i^4}\,K. \tag{9}$$

To numerically determine the time evolution of the bubble radius, $R(t)$, and its radial velocity, $\dot{R}(t)$, for a given function of the pressure imposed in the feeding chamber, $p_c(t)$, Eq. (9) was solved using the MATLAB ODE solver (fourth order Runge-Kutta method), with the initial conditions $R(0)$ and $\dot{R}(0)$ extracted from the

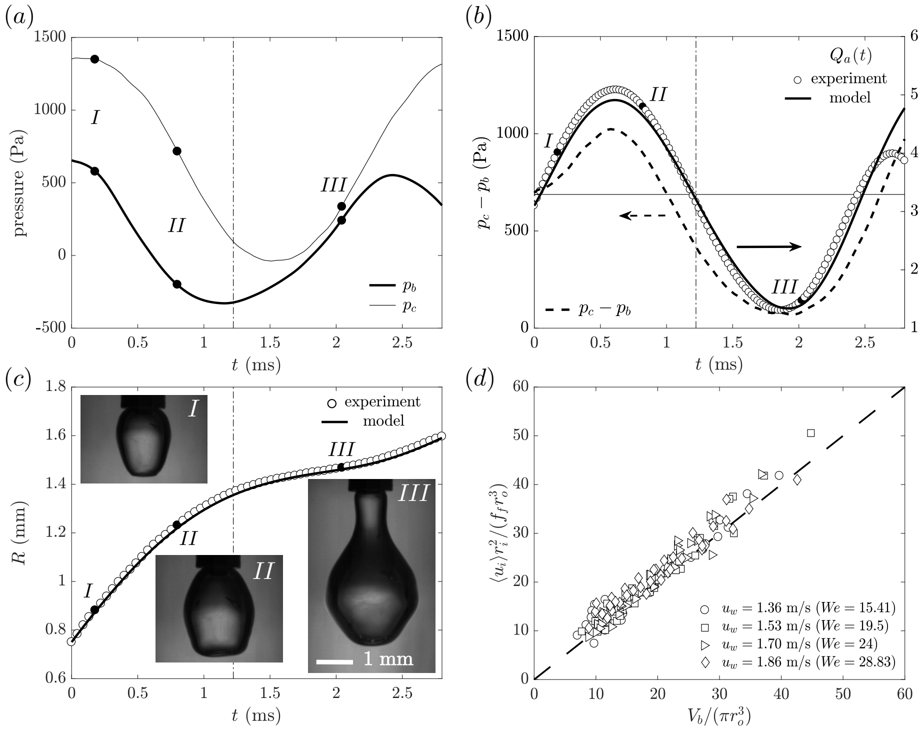

Figure 8: Results obtained from the model computed for a bubbling cycle of the effective bubbling process established for the flow conditions given by $u_a = 4.86$ m/s, $u_w = 1.36$ m/s ($\Lambda = 0.280, We = 15.41$); forced at $f_f = 350$ Hz ($St_f = 0.154$). (a) Temporal evolution of the pressure inside the bubble obtained by the model, $p_b(t)$, together with that of the measured in the feeding chamber, $p_c(t)$. (b) Pressure difference $p_c(t) - p_b(t)$ (dashed line, left axis) and instantaneous gas flow rate, $Q_a(t)$ (solid line, right axis), both calculated from the model. In addition, the gas flow rate obtained experimentally (symbols, right axis) is displayed for comparison. The horizontal line represents the averaged gas flow rate. (c) Comparison of the temporal evolution of the bubble radius obtained from the model and experimentally. In this plot, only one out of two experimental points are plotted for clarity. (d) Dimensionless bubble volume given by the model versus the experimentally obtained from the images for all cases included in this work. The vertical dash-dotted line in plot (a), (b) and (c) represents the end of the expansion stage.

experimental images. Afterwards, the pressure inside the bubble was obtained from Eq. (6). An example of the results given by the model is displayed in Fig. 8, where a complete cycle of an effective bubbling process for $u_a = 4.86$ m/s, $u_w = 1.36$ m/s ($\Lambda = 0.280, We = 15.41$) forced at $f_f = 350$ Hz ($St_f = 0.154$) is shown. The calculated evolution of the pressure inside the bubble, $p_b(t)$, which governs the bubble dynamics, is presented in Fig. 8(a), together with the evolution of the pressure imposed in the feeding chamber, $p_c(t)$. It can be observed that the overall evolution of $p_b(t)$ is similar to that of $p_c(t)$, with some particularities. Firstly, it is clearly shown that, in this case, the bubble pressure, $p_b(t)$, is always lower than $p_c(t)$ although, according to Eqs. (2) and (6), a reverse flow with $p_b > p_c$ could take place at some point under different conditions. Nevertheless, unlike $p_c(t)$, the resulting evolution of $p_b(t)$ is not sinusoidal due to the effects of the dynamics of the growing bubble and the unsteady behaviour of the pressure drop along the needle. Thus, $p_b(t)$ is initially high after the pinch-off of the previous bubble. Such high pressure makes the forming bubble to expand radially very fast, decreasing its pressure, which eventually becomes negative and reaches its minimum value around the end of the expansion phase, when the neck is formed. After this point, the neck begins to collapse and the pressure inside the bubble increases due to the couple effects of the neck closure and the rise of the pressure in the feeding chamber $p_c(t)$. The minimum value of $p_b(t)$ occurs earlier than that in $p_c(t)$, because the initial radial acceleration of the liquid surrounding the bubble makes the pressure inside the bubble decrease faster than that in the chamber to supply the gas flow rate required

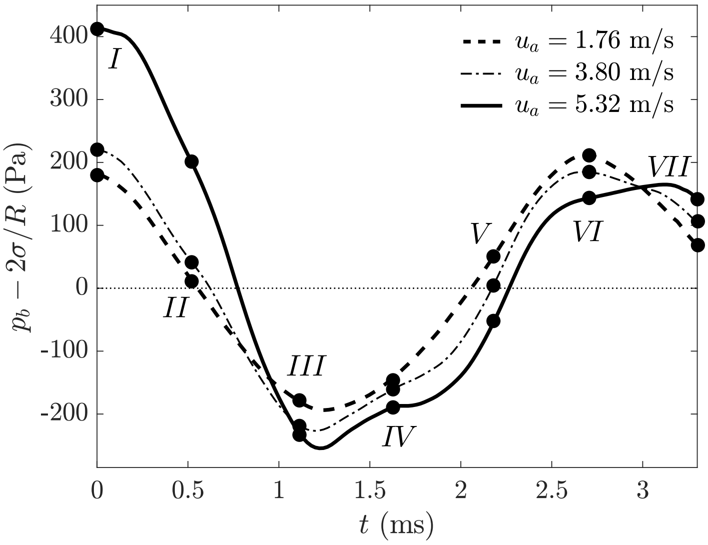

Figure 9: Temporal evolution of the pressure at the liquid interface during a forcing cycle for the experimental conditions shown in Fig. 3 ($u_w = 1.36$ m/s, $f_f = 300$ Hz).

by the bubble growth, $Q_a(t) = dV(t)/dt$, as observed in Fig. 8(b). The reduction of pressure inside the bubble decelerates the outer liquid, reducing the decreasing rate of $p_b(t)$ and, thus the air flow rate since $p_c(t)$, driven by the loudspeaker, continues decreasing. After reaching the minimum value, $p_b(t)$ starts to increase to accommodate the gas flowing from the feeding chamber. However, the slow increasing rate of the pressure together with the inertia of the liquid surrounding the neck region contribute to accelerate the closure of the neck and, consequently the bubble pinch-off.

The difference between $p_c(t)$ and $p_b(t)$ and the resulting time evolution of the gas flow rate, $Q_a(t)$ are plotted in Fig. 8(b). As expected, both curves follow the same trend but, more importantly, it should be noticed the excellent agreement between the time evolution of $Q_a(t)$ provided by the model and that obtained experimentally over nearly the entire bubbling period. Only during the final moments of the cycle does the model fail due to the limitations inherent in its formulation. One of them is that the model does not include the local closing process of the neck due to the spherical assumption of the bubble shape during the entire bubbling process. An additional limitation is that the model is an incompressible one, and cannot account for the rapid increase of pressure inside the bubble caused by compressible effects occurring when the neck closure is very fast, especially at low values of Λ. Such limitations reduce the capability of the model to accurately reproduce the increase of pressure which takes place just before the collapse of the neck and the associated flow rate decrease, observed experimentally. Furthermore, Fig. 8(c) shows the evolution of the computed value of $R(t)$ (solid line), together with the equivalent bubble radius from the experimental images (symbols), obtained as $[3\,V(t)/(4\pi)]^{1/3}$. Notice that the bubble continuously grows during the whole cycle, showing a faster inflation rate during the expansion stage, whose duration is indicated by a vertical dash-dotted line in Figs. 8(a), (b) and (c). The general evolution of the air flow rate is well estimated, validating the proposed model and indicating that it nearly reproduces the dynamics of the process during the entire bubbling event. Figure 8(c) also includes three snapshots, denoted as I, II and III in panels (a), (b) and (c) to help to associate the bubble shape with the pressure inside the bubble and the injected flow rate. From instant I to II the pressure inside the bubble decreases rapidly and the bubble inflates. After reaching the minimum value, a neck begins to form and propagate downstream as it closes, at the same time that the bubble pressure increases (point III).

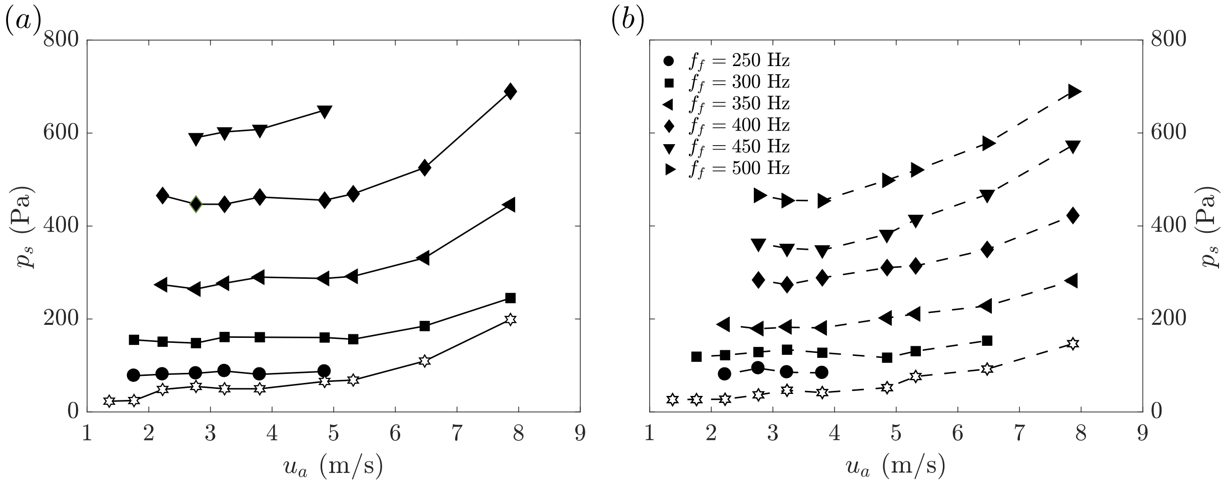

Figure 10: Dependence of p_s with the air velocity for different values of the forcing frequency at (a) $u_w = 1.53$ m/s ($We = 19.5$) and (b) $u_w = 1.86$ m/s ($We = 28.83$). The hollow symbols correspond to the unforced cases and the solid ones to forced cases.

In order to check the validity of the model for the entire range of the parameters explored in the work, Fig. 8(d) shows the final bubble volume given by the model as the averaged air flow rate injected during the forcing period, $\langle u_i \rangle \pi r_i^2 / f_f = \int_0^{1/f_f} Q_a(t)\,\mathrm{d}t$, against the volume of the detached bubble obtained from the experimental images as $V_b = V(1/f_f) - V(0)$, both made dimensionless with (πr_o^3). The good agreement between the results given by the model and the experimental ones corroborates the capability of the proposed model. Thus, the measurements of $p_c(t)$ and the initial conditions, namely $R(0)$ and $\dot{R}(0)$, will be used in the following section to model the time evolution of the pressure inside the bubble $p_b(t)$ during the forced bubbling cycle under the critical pressure amplitude Δp_c^c.

5. Scaling of the effective pressure amplitude and of the initial radial velocity

The model described in Section 4 has been used to determine the time evolution of the pressure inside the bubble, $p_b(t)$, knowing the pressure in the feeding chamber, $p_c(t)$. Thus, the mean value and the characteristic pressure amplitude required to generate bubbles at the forcing frequency can be obtained. As an example, the time evolution of the pressure at the liquid side of the interface, $p_b(t) - 2\sigma/R$, is shown in Fig. 9 for the three cases displayed in Fig. 3. The figure illustrates that the temporal evolutions of the pressure are very similar, with the maximum value taking place at the beginning of the cycle. It also shows that the amplitude increases with the air velocity and, since the forced bubbling cycle has the same duration for the three cases, there is a faster decreasing rate of the pressure when u_a increases, while the mean values of the pressure, $\bar{p}_b$, are very similar. To characterize the pressure amplitude that needs to be established inside the bubble to have a bubbling frequency equal to the forcing one, the root-mean-square of $p_b(t)$ will be used,

$$p_s = \sqrt{f_f \int_0^{1/f_f} \left[p_b(t) - \bar{p}_b\right]^2 \, dt}, \tag{10}$$

where $\bar{p}_b$ indicates the mean value of $p_b(t)$. Figure 10 shows the dependence of p_s with the air velocity and the forcing frequency for two different water velocities. It is clearly seen that, to generate bubbles at the forcing frequency, the critical pressure amplitude increases substantially with the forcing frequency and decreases with the water velocity. However, its dependence with the air velocity is not monotonic. In particular, for all the forcing frequencies, p_s barely changes at low air velocities, while it increases with u_a for larger values of the air velocity. The same behavior has been observed for the rest of the water velocities

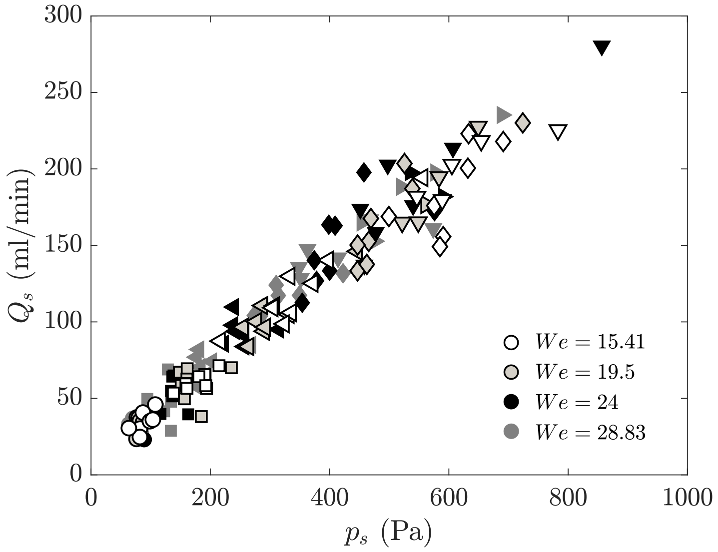

Figure 11: Dependence of the root-mean-square of the gas flow rate feeding the bubble, Q_s, with the root-mean-square of the pressure inside the bubble, p_s, for all the experiments performed in this work. Different types of symbols indicate different forcing frequencies as in Fig. 10.

tested. Note that, the bubbling process could also be controlled by perturbing the injected gas flow rate instead of the pressure in the air feeding chamber. In this case, the flow rate amplitude would be a practical control parameter to drive the bubbling process. Thus, we have represented in Fig. 11 the root-mean-square of the gas flow rate feeding the bubble, Q_s, obtained experimentally during a bubbling period, versus p_s, observing a linear dependence of Q_s with p_s. Consequently, in the following we will focus on determining the critical pressure amplitude required to control the bubble generation process, i.e. $p_s(f_f, u_w, u_a)$, having in mind that the analysis is also valid to obtain $Q_s(f_f, u_w, u_a)$ from Fig. 11.

The dependence of p_s with u_a can be explained in terms of the overpressure generated inside the forming bubble by the dynamics of the neck closure. To analyse this effect, we will first focus on the natural bubbling cases, where there is no additional effect of the forcing frequency. Figure 12(a) shows the time evolution of both the pressure at the liquid interface and the instantaneous air flow rate minus the averaged one, $(Q_a(t) - Q_c)$, obtained experimentally during two bubbling cycles for $u_w = 1.36$ m/s and two different values of u_a. To better compare the two cases, since the bubbling frequencies are different, the time has been normalized with the formation frequency, f_b. On the one hand, for large values of u_a (black solid line and down triangles), when a bubble pinches off, the neck closes very fast, driven by the Bernoulli suction effect (Gordillo et al., 2005; Bergmann et al., 2009). Thus, the gas stream must suddenly stop, increasing the pressure at the initial instants of the following cycle to values of the order of those occurring in a *water hammer* phenomenon, $p_b(t = 0) \sim \rho_a \, c \, u_a$, where c is the speed of sound in air (or the speed of the elastic wave). This overpressure coincides with the rapid decrease of the air flow rate that takes place between the end of a cycle and the beginning of the following one at times of the order of the acoustic one, as shown in Fig. 12(a), and in agreement with Sevilla et al. (2005). As the new forming bubble expands, the volume growth rate increases while the pressure rapidly decreases, reducing the outward radial velocity. Eventually, the liquid interface pressure becomes negative, leading to a local inward radial motion of this interface, which gives rise to the collapse stage (Gordillo et al., 2007). On the other hand, for smaller values of u_a (grey dashed line and circles), the air velocity is closer to that of the water, leading to a slower neck closure with a lower air flow towards the forming bubble during the latest instants of the collapse process. In this case, Fig. 12(a) shows a smooth evolution of the air flow rate from a cycle to the following one, without

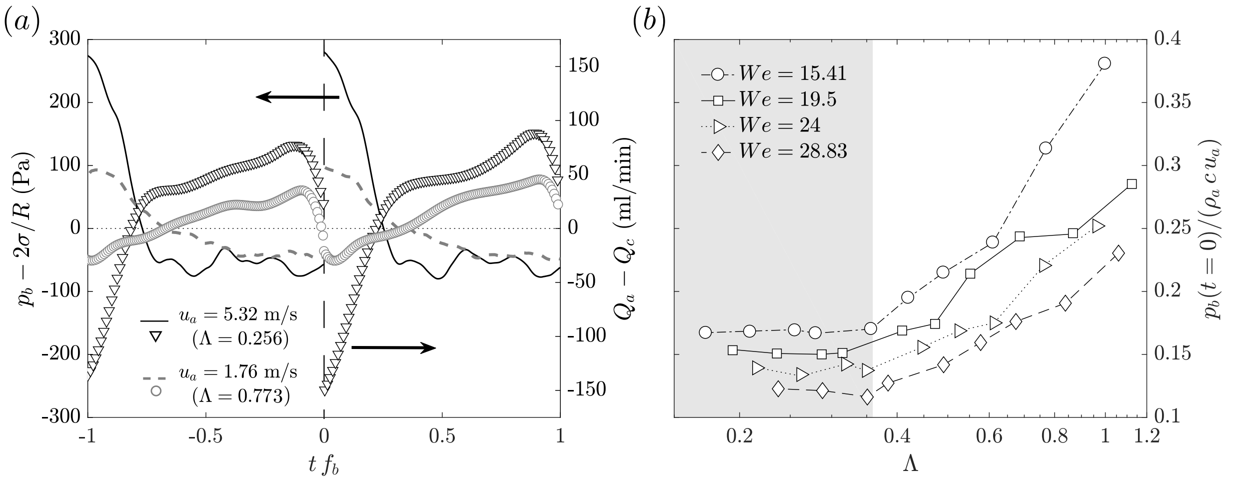

Figure 12: (a) Temporal evolution of the pressure at the liquid interface (lines, left axis) and the fluctuating flow rate, $Q_a(t) - Q_c$ (symbols, right axis), during two unforced bubbling cycles for $u_w = 1.36$ m/s ($We = 15.41$) and two air velocities. The vertical long-dashed line indicates the instant at which the bubble pinch-off takes place. (b) Dependence of the dimensionless instant pressure inside the bubble at t=0, $p_b(t=0)/(\rho_a c u_a)$, with Λ, for the unforced cases at different Weber numbers. The shaded region corresponds to the range of values of Λ for which the overpressure is generated by a rapid closure of the neck (*water hammer* phenomenon).

observing a discontinuity at the pinch-off instant. Therefore, the initial overpressure that triggers the expansion of the new bubble is induced by a mechanism different from that associated to a *water hammer*. Indeed, as suggested by Gordillo et al. (2005), during the latest instants of the bubble collapse, the air flow rate through the neck is reduced, leading to gas accumulation in the ligament. This makes the pressure in the ligament increase and, consequently, the air flow rate from the gas-feeding chamber decrease, as it is shown in Fig. 12(a) just prior to the pinch-off time.

In order to determine the conditions under which the initial overpressure is driven by each mechanism, Fig. 12(b) represents the value of the bubble initial overpressure obtained from the model $p_b(t=0)$ for the natural cases, divided by $(\rho_a\, c\, u_a)$, i.e. the pressure associated to an instantaneous closure, as a function of Λ. It can be seen that there are two different regions depending on the value of Λ. In the first region, for $\Lambda < 0.36$, highlighted by the shaded area in Fig. 12(b), the dimensionless overpressure remains constant with Λ, and only depends on We. The overpressure in these cases is generated by the rapid closure of the neck, being of the order of that caused by a *water hammer*. However, in the second region, $p_b(t=0)$ barely changes with the air velocity, as occurs with p_s at low values of u_a in Fig. 10 and, thus, the dimensionless overpressure increases as u_a decreases, or similarly, as Λ increases (see the unshaded area in Fig. 12b). This trend reveals that, for $\Lambda > 0.36$, the pinch-off is driven by a slower closure of the neck, with an initial overpressure almost independent of the air velocity. Since in the natural cases there is no artificially induced pressure variation, the pressure values only reflect the influence of u_a and of the collapse velocity. Therefore, the transitional value of the water-to-air velocity ratio, at which the dominant mechanism changes, i.e. $\Lambda \approx 0.36$, will remain the same for the forced cases, as previously suggested by Figs. 4(d) and (f).

Taking into account the results displayed in Fig. 12(b), we will first focus on the pressure amplitude, given by p_s for $\Lambda < 0.36$. Thus, we have represented the mean value of the dimensionless pressure amplitude $\langle\, p_s/(\rho_a c u_a)\,\rangle$ versus the forcing Strouhal number in Fig. 13(a) for the four different water velocities, or Weber numbers, used in this work. It has to be pointed out that for each value of St_f, $\langle\,\rangle$ denotes the averaged value obtained for $\Lambda < 0.36$, for which the dimensionless pressure amplitude remains nearly constant, while the error bars in Fig. 13(a) represent the standard deviation. It can be seen that the dimensionless pressure

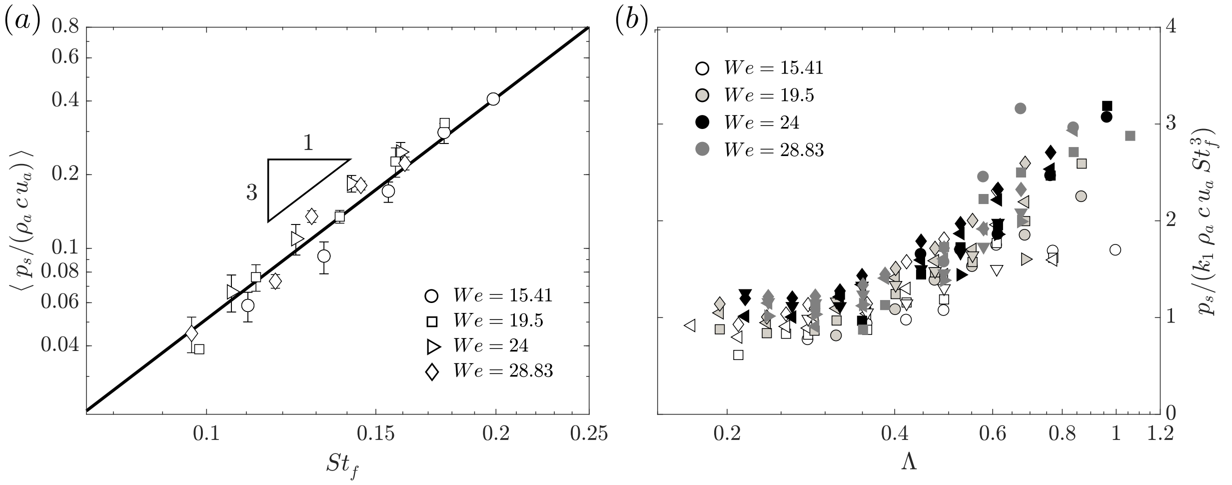

Figure 13: (a) Doubly logarithmic plot of the dimensionless pressure amplitude, averaged in the range $\Lambda < 0.36$, as a function of the forced Strouhal number. Symbols correspond to the averaged values and error bars to their standard deviations. The best data fit, given by the function St_f^3, is displayed with a solid line. (b) Amplitude of the pressure perturbation inside the bubbles, p_s, scaled by Eq. (11) with $k_1 = 50.43$, for the four values of the water velocities (or Weber numbers) studied. Different symbols indicate different forcing frequencies, as in Fig. 10.

amplitude increases with the Strouhal number as St_f^3. Thus, the overpressures generated inside the forming bubbles are indeed caused by the rapid closure of the neck, with an additional contribution due to the law that governs the closing of the neck which is taken into account by the Strouhal number. Consequently, the pressure amplitude that needs to be established inside the bubble to control the bubbling process is given by,

$$p_s = k_1\, \rho_a\, c\, u_a\, St_f^3. \tag{11}$$

Figure 13(b) shows p_s normalized as indicated by Eq. (11) for the entire range of values of Λ. Two different regions can be distinguished; for $\Lambda \lesssim 0.36$, all the points collapse on a constant value, while for $\Lambda \gtrsim 0.36$, an additional dependence with Λ is observed. The collapse of all the data points on a constant value for $\Lambda < 0.36$ indicates that Eq. (11), with $k_1 = 50.43$, is a good estimation of p_s in that range of water-to-air velocity ratios. Thus, it is confirmed that a compressible mechanism, caused by the rapid closure of the neck, drives the process for low enough values of Λ (or large air velocities). This is in agreement with the temporal evolution of $Q_a(t)$ shown in Figs. 4(d) and (e), where it can be observed a sudden decrease of Q_a from the end of a cycle to the beginning of the following one occurring at times of the order of the acoustic one. However, the dependence of $p_s/(\rho_a c u_a St_f^3)$ with Λ shown in Fig. 13(b) for $\Lambda \gtrsim 0.36$ indicates that there is a different mechanism governing the pressure increase that needs to be generated inside the bubbles to control the bubbling process.

In fact, the same conjecture can be raised from Fig. 10, where it is shown that p_s does not longer depend on u_a at low values of the air velocity (large values of Λ). In these cases, a slow increment of pressure due to gas accumulation upstream from the neck dominates over the weak neck closing effect. Consequently, a new model has to be proposed to scale p_s at large values of Λ. Thus, from now on we will consider only the cases of $\Lambda > 0.36$. In these cases, where the air velocity is closer to that of the water, the closure of the neck is slower than in the cases of small Λ. Then, the pressure gradients along the intact ligament, of length l_i, during the collapse time, that generates the initial radial expansion of the bubble, can be estimated, using incompressible theory, as $p_s/l_i \sim \rho\, r_o/t_{col}^2$, giving

$$p_s \sim \rho\, u_w^2\, \frac{r_o}{l_i}, \tag{12}$$

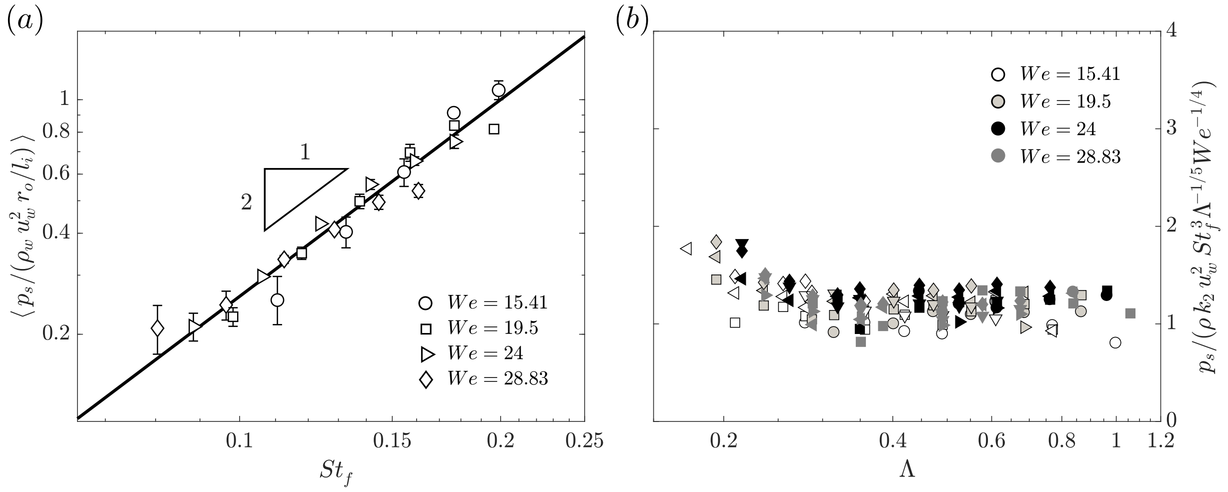

Figure 14: (a) Dependence of $p_s/(\rho u_w^2 r_o/l_i)$ with St_f, represented in logarithmic scale, for the four values of the water velocities (or Weber numbers) studied and $\Lambda > 0.36$. Symbols correspond to the averaged value over the selected experiments, being the error bars the standard deviation. The solid line represents the best data fit, having this function a nearly quadratic dependence, $\propto St_f^2$. (b) Amplitude of the pressure perturbation inside the bubbles, p_s, scaled with the expression given by Eq. (14) with $k_2 = 64.13$, for all the experiments performed in this work. Different types of symbols indicate different forcing frequencies as in Fig. 10.

where $t_{col} \simeq l_i/u_w$ is the collapse time of the neck (Ruiz-Rus et al., 2020). Since p_s has been also observed to depend on the forcing frequency (see Fig. 10), $\langle p_s/(\rho u_w^2 r_o/l_i) \rangle$ is displayed as a function of St_f for the cases where $\Lambda > 0.36$ in Fig. 14(a). Here, $\langle \, \rangle$ now indicates the averaged values for $\Lambda > 0.36$, for each value of St_f, with the standard deviation depicted as error bars. The figure shows a good collapse of the experimental data with a quadratic dependence with the Strouhal number, St_f^2. Consequently, it can be deduced that,

$$p_s \sim \rho \, u_w^2 \, St_f^2 \, \frac{r_o}{l_i}. \tag{13}$$

Moreover, l_i/r_o can be determined from Ruiz-Rus et al. (2020) as $l_i/r_o \propto St_f^{-1} \Lambda^{1/5} We^{1/4}$. Substituting this expression into Eq. (13), one gets

$$p_s = k_2 \, \rho \, u_w^2 \, St_f^3 \, \Lambda^{-1/5} \, We^{-1/4}. \tag{14}$$

Figure 14(b) displays p_s scaled with Eq. (14) as a function of Λ, revealing that all the experiments for $\Lambda \gtrsim 0.36$ collapse on a nearly constant value, with $k_2 = 64.13$. This result indicates that Eq. (14) provides a proper scaling in this range of values of Λ. At the same time, it confirms that the proposed mechanism of a slow neck closure generates the required bubble pressure amplitude when the air velocity is not sufficiently high to produce a sudden increase of pressure, as occurs for $\Lambda \lesssim 0.36$. Thus, since the tip of the intact ligament moves downward at the water velocity, the air stream discharges in an environment whose volume increases at a rate similar to the incoming flow rate. Consequently, the pressure inside the air ligament is driven by the closing law of the neck, what barely depends on the air velocity, but it is connected with the forcing frequency.

As described above, two different behaviors have been observed depending on the water-to-air velocity ratio, Λ. On the one hand, at low values of Λ, when a bubble is about to pinch off, the neck closes very fast, generating an increase of pressure that resembles that generated in a *water hammer* phenomenon. However, the value of p_s that needs to be established in the bubble is modulated by the forced Strouhal number, with a power law given by St_f^3. This dependence is a consequence of the closing law of the neck, that can be

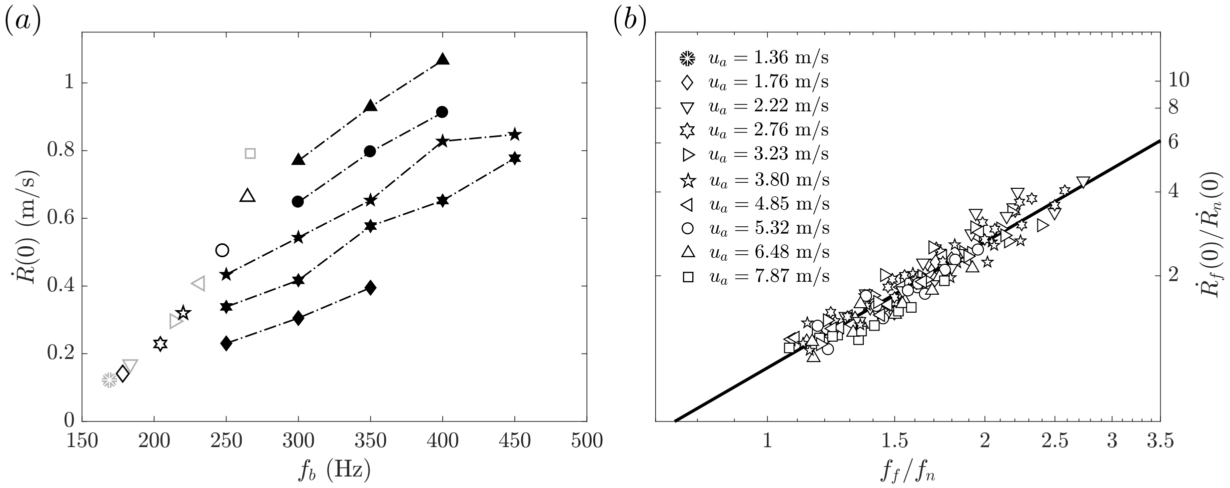

Figure 15: (a) Effect of the bubbling frequency, f_b, on the initial radial expansion velocity, $\dot{R}(0)$, for $u_w = 1.36$ m/s. Hollow and solid symbols indicate unforced and forced cases respectively. (b) Forced-to-unforced initial radial expansion velocity, $\dot{R}_f(0)/\dot{R}_n(0)$ with respect to the forced-to-unforced bubbling frequency, f_f/f_n. The solid line shows that $\dot{R}_f(0)/\dot{R}_n(0) = (f_f/f_n)^{3/2}$.

written as $r_n \propto (t_c - t)^n$, where $r_n(t)$ is the radius of the neck, t_c the closing time and n an exponent that depends on St_f. In fact, an instantaneous neck closure would induce a pressure increase of the order of $p_s \sim \rho_a\, c\, u_a$, where c is the sound speed or the speed of propagation of the pressure waves traveling along the air ligament. A detailed study of the closing process of the neck and its dependence with Λ, We and, more importantly, with St_f could provide the proper increase of pressure generated in the forming bubble after the pinch-off of the previous one. Nevertheless, such study is out of the scope of the present work, and the effect of the forcing frequency was included in Eq. (11) through the Strouhal number. It has to be pointed out that, in Eq. (11), the constant $k_1 = 50.43$ is apparently too high simply because the forcing frequency has been used in St_f instead the inverse of the closing time, since $St_f \ll r_o/(u_w t_c)$. On the other hand, at higher Λ values, the air velocity is closer to that of water, and the air ligament elongates at a speed that allows the gas flow to be accommodated. In theses cases, the neck closure is much slower than at lower values of Λ, and the compressible mechanism caused by a *water hammer* phenomenon no longer takes place. Instead, the mechanism generating the pressure increase that is required in the forming bubble to control the bubbling process is mainly an incompressible one. Specifically, part of the incoming flow fills the bubble that is about to pinch off and the rest remains in the air ligament, being the germ of the next bubble. When the neck closes, the incoming air flow makes the pressure increase to inflate the ligament at a rate such that its variation of volume is equal to $Q_a(t)$. Although the value of Λ that defines the separation of both regimes might depend on the Weber number, in the range of values of We explored in this work, it has been found to be $\Lambda \approx 0.36$. In fact, matching Eqs. (11) and (14), a weak dependence of the transitional value of Λ can be found with We, as $We^{-5/16}$,

$$\Lambda_t = \left(\frac{k_1}{k_2}\right)^{5/4} \left(\frac{\rho_a}{\rho}\right)^{5/4} \left(\frac{\rho\, c^2 r_o}{\sigma}\right)^{5/8} We^{-5/16}, \tag{15}$$

whose mean value is $\Lambda_t = 0.35$.

To conclude this Section, we will describe the mechanisms leading to the initial expansion of the bubble with the aim at providing a proper expression for the initial radial bubble velocity required, as initial condition, to implement the model described in Section 4. A close inspection of Figs. 3 and 9 indicates that the maximum value of the pressure inside the bubbles always occurs at the beginning of the bubbling

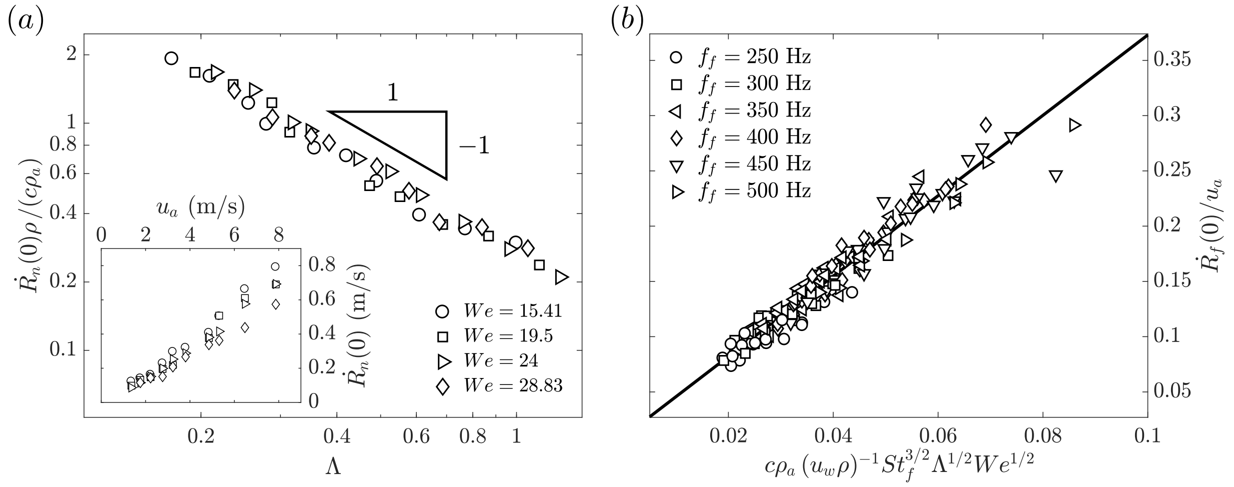

Figure 16: (a) Dependence of the initial radial expansion velocity of the unforced cases, $\dot{R}_n(0)$ divided by $\rho_a c/\rho$ with Λ. The figure shows a collapse of all the experimental point, indicating that $\dot{R}_n(0)\rho/(\rho_a\, c) \propto \Lambda^{-1}$ (b) Experimental validation of Eq. (18) with $k^* = 3.637$.

process, inducing a rapid radial acceleration of the outer liquid. In fact, as mentioned above, at low values of $\Lambda = u_w/u_a$, where the air velocity is larger than that of the water, when a bubble pinches off, the neck closes very fast. Thus, the gas stream must suddenly stop, increasing the pressure at $t = 0$ to values of the order of those occurring in a *water hammer* phenomenon. This overpressure causes the expansion of the intact ligament with an initial velocity that we will denote $\dot{R}(0)$. The experimental values of $\dot{R}(0)$ have been represented in Fig. 15(a) for u_w=1.36 m/s. It can be seen that, in the unforced cases displayed by hollow symbols, $\dot{R}_n(0)$ increases with the bubbling frequency, f_b. However, when the bubbling process is controlled by the forcing system, $\dot{R}_f(0)$ increases with the forcing frequency, even for equal values of u_a, being always larger than the corresponding natural case since $f_f > f_n$. Moreover, comparing the initial radial expansion velocities obtained in the forced cases, $\dot{R}_f(0)$ with those in the unforced ones, $\dot{R}_n(0)$, it was found that

$$\frac{\dot{R}_f(0)}{\dot{R}_n(0)} \propto \left(\frac{f_f}{f_n}\right)^{3/2}, \tag{16}$$

as displayed in Fig. 15(b).

Interestingly, this figure shows that all the experimental measurements, performed varying u_w, u_a and f_f, collapse onto the same curve, described by Eq. (16). Since, at large values of u_a (low values of Λ), the liquid accelerates radially during times of the order of the acoustic time, $\dot{R}_n(0)$ can be estimated as $\dot{R}_n(0) \sim (\rho_a/\rho)\, c\, u_a t_c/r_o$, where $t_c \sim L/c \sim 30\, r_o/30\, u_a \sim r_o/u_a$, giving $\dot{R}_n(0) \sim (\rho_a/\rho)\, c$. To corroborate this hypothesis, Fig. 16(a) shows the initial radial expansion velocity of the bubbles versus the water-to-air velocity ratio indicating that,

$$\frac{\rho \dot{R}_n(0)}{\rho_a\, c} \propto \Lambda^{-1}, \tag{17}$$

what indeed indicates that $\rho_a\, c\, u_a \sim \rho\, u_w\, \dot{R}_n(0)$. Substituting Eq. (17) into Eq. (16), one gets

$$\frac{\dot{R}_f(0)}{u_a} = k^* \left(\frac{\rho_a\, c}{\rho\, u_w}\right) St_f^{3/2}\, \Lambda^{1/2}\, We^{1/2}, \tag{18}$$

where $St_f = f_f r_o/u_w$ and $St_n = f_n r_o/u_w$ are the Strouhal numbers based on the bubbling frequency, which is f_f in the forced cases, and f_n in the natural unforced ones and, according to Ruiz-Rus et al. (2020),

$St_n \propto (\Lambda We)^{-1/3}$. Expression (18) has been verified experimentally in Fig. 16(b), showing an excellent agreement with $k^* = 3.637$. Thus, the initial radial expansion velocity, to be used in the model descibed in Section 4, is given by,

$$\dot{R}_f(0) = k^* \left(\frac{\rho_a}{\rho}\right) c\, St_f^{3/2}\, \Lambda^{-1/2}\, We^{1/2}. \tag{19}$$

6. Conclusions

In this work, we have determined the gas pressure and flow rate amplitudes which are required to generate inside the bubbles to produce them at a given frequency in a co-flowing gas-liquid jet. To that aim, we performed experiments, where a harmonic pressure perturbation with a forcing frequency, f_f, was applied in the air feeding chamber with a loudspeaker. The air pressure inside the chamber where the perturbations were induced, $p_c(t)$, was registered with a pressure sensor synchronized with a high-speed camera, used to record the time evolution of the bubble interface. Thus, the instantaneous gas flow rate, $Q_a(t)$, driven by the pressure modulation, was experimentally measured from image processing. It has been shown that, when the pressure amplitude inside the bubble is high enough, the bubbling process is controlled by the forcing system, generating monodisperse bubbles at the forcing frequency. Since the forcing frequency is larger than the natural one, $f_f > f_n$, smaller bubbles are produced. Consequently, for each natural case, defined by the values of (u_a, u_w), and a given f_f, we slowly increased the pressure amplitude until bubbles were periodically generated at the forcing frequency, finding the minimum effective or critical pressure amplitude, Δp_c^c, required for the forcing mechanism to control the process.

However, since in this case $\Delta p_c^c(u_w, u_a, f_f)$ represents the critical pressure amplitude in the air feeding chamber required in our facility, a model to calculate the pressure inside the forming bubble, $p_b(t)$, has also been developed. Hence, a general criterion, applicable to a different facility, has been established. In particular, the growing bubble has been modeled by the inviscid spherical Rayleigh-Plesset equation, together with the oscillatory and incompressible gas flow along the injecting needle, obtaining a very good agreement between the values of $Q_a(t)$ given by the model and the experimental results. Once the time evolution of the pressure inside the forming bubble was determined, the amplitude required to control the bubbling process has been characterized by the root-mean-square of $p_b(t)$, denoted p_s.

Interestingly, depending on the water-to-air velocity ratio, Λ, two different mechanisms leading to the increase of pressure inside the forming bubble, required to control the process, have been observed. For $\Lambda < 0.36$, during the latest instants of the bubble formation process, the neck collapses rapidly, generating an increase of pressure similar to what happens in a *water hammer* phenomenon. However, the value of p_s that needs to be established in the bubble also depends on the forced Strouhal number, with a power law given by St_f^3. For $\Lambda > 0.36$, the neck closure is much slower than at lower values of Λ, and the initial increase of pressure, required to control the bubbling process, is caused by an incompressible mechanism. Indeed, a portion of the gas injected feeds the forming bubble, while the rest remains in the air ligament of the following bubble. When the neck closes, the incoming airflow makes the pressure inside the intact ligament increase, causing the ligament to inflate at the rate necessary to accommodate the airflow, $Q_a(t)$.

CRediT authorship contribution statement

J. Ruiz-Rus: Conceptualization, Methodology, Software, Investigation, Visualization, Writing - original draft. **R. Bolaños-Jiménez:** Conceptualization, Supervision, Writing - review & editing, Funding acquisition. **A. Sevilla**: Conceptualization, Supervision, Writing - review & editing. **C. Martínez-Bazán:** Conceptualization, Supervision, Project administration, Writing - review & editing, Funding acquisition.

Declaration of Competing Interest

The authors declare that they have no known competing financial interests or personal relationships that could have appeared to influence the work reported in this paper.

Acknowledgments

This work has been supported by the Spanish MINECO and European Funds under projects DPI2017-88201-C3-2-R and DPI2017-88201-C3-3-R. JRR wants to acknowledge the Spanish MINECO for the financial support provided by the Fellowship BES-2015-071329. Support from the Red Nacional para el Desarrollo de la Microfluídica, RED2018-102829-T, is also acknowledged.

References

Bergmann, R., Andersen, A., Van der Meer, D., Bohr, T., 2009. Bubble pinch-off in a rotating flow. Phys. Rev. Lett. 102, 204501.

Chuang, S.C., Goldschmidt, V.W., 1970. Bubble formation due to a submerged capillary tube in quiescent and coflowing streams. J. Basic Engng. 92, 705–711.

Cummings, A., 1986. Transient and multiple frequency sound transmission through perforated plates at high amplitude. J. Acoust. Soc. Am. 79, 942–951.

García, F.J., González, H., Castrejón-Pita, J.R., Castrejón-Pita, A.A., 2014. The breakup length of harmonically stimulated capillary jets. App. Phys. Lett. 105, 094104.

Gordillo, J.M., Sevilla, A., Martínez-Bazán, C., 2007. Bubbling in a co-flow at high Reynolds numbers. Phys. Fluids 19, 077102.

Gordillo, J.M., Sevilla, A., Rodríguez-Rodríguez, J., Martínez-Bazán, C., 2005. Axisymmetric bubble pinch-off at high Reynolds numbers. Phys. Rev. Lett. 95, 194501.

Higuera, F.J., Medina, A., 2006. Injection and coalescence of bubbles in a quiescent inviscid liquid. Eur. J. Mech. B 25, 167–171.

Howe, M.S., 1998. Acoustics of fluid-structure interactions. Cambridge university press.

Kumar, R., Kuloor, N.K., 1970. The formation of bubbles and drops. Adv. Chem. Eng. 8, 255–368.

Lichtarowicz, A., Duggins, R.K., Markland, E., 1965. Discharge coefficients for incompressible non-cavitating flow through long orifices. J. Mech. Engng. Sci. 7, 210–219.

Luong, T., Howe, M.S., McGowan, R.S., 2005. On the Rayleigh conductivity of a bias–flow aperture. J. Fluids Struct. 21, 769–778.

Maier, C.G., 1927. Producing small bubbles of gas in liquids by submerged orifices. U. S. Bur. Mines Bull. 260.

Oğuz, H.N., Prosperetti, A., 1993. Dynamics of bubble growth and detachment from a needle. J. Fluid Mech. 257, 111–145.

Rayleigh, J.W.S., 1945. The theory of sound. Dover, New York.

Rodríguez-Rodríguez, J., Sevilla, A., Martínez-Bazán, C., Gordillo, J.M., 2015. Generation of microbubbles with applications to industry and medicine. Annu. Rev. Fluid Mech. 47, 405–429.

Ruiz-Rus, J., Bolaños-Jiménez, R., Gutiérrez-Montes, C., Sevilla, A., Martínez-Bazán, C., 2017. Controlled formation of bubbles in a planar co-flow configuration. Int. J. Multiphase Flow 89, 69–80.

Ruiz-Rus, J., Bolaños-Jiménez, R., Sevilla, A., Martínez-Bazán, C., 2020. Bubble formation regimes in forced co-axial air-water jets. Int. J. Multiphase Flow 128, 103296.

Sevilla, A., Gordillo, J.M., Martínez-Bazán, C., 2005. Bubble formation in a coflowing air–water stream. J. Fluid Mech. 530, 181–195.

Yellin, E.L., Peskin, C.S., 1975. Large amplitude pulsatile water flow across an orifice. J. Dyn. Syst. - T. ASME 97, 92–95.